Journal of Electroanalytical Chemistry 999 (2025) 119580

Contents lists available at ScienceDirect

Journal of Electroanalytical Chemistry

journal homepage: www.elsevier.com/locate/jelechem

Hierarchical assembled sulfur-doped Mo—Fe polyoxometalate/ZIF-67 on Ni foam: A novel and efficient electrocatalyst for water splitting and urea oxidation

Zhwan Naghshbandi [a,*], Abdollah Salimi [a,b,*], Ali Feizabadi [c]

[a] Department of Chemistry, University of Kurdistan, Sanandaj 66177-15175, Iran
[b] Research Center for Nanotechnology, University of Kurdistan, Sanandaj 66177-15175, Iran
[c] Department of Chemistry, University of Western Ontario, London, ON, Canada

ARTICLE INFO

Keywords:
Polyoxometalate (POM)
Electrocatalysis
Water splitting
Hydrogen evolution reaction (HER)
Urea oxidation reaction (UOR)
Oxygen evolution reaction (OER)
Sulfur doping

ABSTRACT

Electrocatalytic water splitting is a promising method for high-efficiency hydrogen (H_2) production, providing a clean and sustainable alternative to fossil fuels. However, the development of efficient, cost-effective, and durable nonprecious metal electrocatalysts for both the oxygen evolution reaction (OER) and hydrogen evolution reaction (HER) remains a significant challenge. In this study, a novel electrocatalyst-sulfur-doped iron polyoxometalate (Fe-POM-S) decorated with zeolitic imidazolate frameworks (ZIF-67) on nickel foam (NF)-was synthesized via a straightforward multi-step process. Comprehensive characterization confirmed the morphology, crystal structure, and elemental composition of the NF/Fe-POM-S/ZIF-67 catalyst. The catalyst showed excellent performance under alkaline conditions for both electrocatalysis and photoelectrocatalysis. It achieved an overpotential of 190 mV for OER under light and 130 mV for HER after calcination at 500 °C, both at 10 mA cm^{-2}. Overall water splitting required a low cell voltage of 1.5 at a current density of 10 mA cm^{-2}. For urea oxidation (UOR) in 1.0 M KOH with 0.5 M urea, the catalyst achieved 10 mA cm^{-2} at only 1.33 V, with overall urea electrolysis requiring 1.38 V. Notably, the catalyst exhibited exceptional durability, retaining activity for over 48 h with negligible performance loss at current density of 100 mA cm^{-2}. This work presents a facile synthesis strategy for designing high-performance, stable electrocatalysts and photoelectrocatalysts, with significant potential for renewable energy applications.

1. Introduction

The global energy crisis, environmental degradation, and reliance on fossil fuels necessitate the urgent development of sustainable and renewable energy sources. Hydrogen, as a clean energy carrier with high energy density and zero carbon emissions, is considered a promising alternative to conventional fossil fuels [1–4]. However, current industrial hydrogen production methods, such as steam methane reforming and coal gasification, are unsustainable and contribute significantly to CO_2 emissions. Among the various approaches for hydrogen production, water splitting driven by electrochemical and photoelectrochemical methods has garnered significant attention due to its ability to produce high-purity hydrogen in an environmentally friendly manner [5–9]. Despite this potential, the development of efficient and cost-effective electrocatalysts for the oxygen evolution reaction (OER) and hydrogen evolution reaction (HER), the two half-reactions of water splitting, remains a critical challenge. Photoelectrochemical water splitting, utilizing sunlight and a suitable photocatalyst, is employed to convert water molecules into O_2 and H_2. When light shines on a photocatalyst, an electron is excited from the valence band (VB) to the conduction band, generating electronic charge carriers, including electrons (e^-) and holes (h+), at the anode. At the anode, the holes generated lead to the conversion of water into O_2, and the electrons produced via external circuits are transferred to the cathode [10–17].

Platinum-based catalysts for HER and Iridium- or Ruthenium-based catalysts for OER have shown outstanding activity; however, their high cost, rarity, and limited long-term stability hinder large-scale use [18–20]. As a result, researchers are focusing on developing earth-abundant, nonprecious metal catalysts with equal or better performance.

* Corresponding authors at: Department of Chemistry, University of Kurdistan, Sanandaj 66177-15175, Iran.
E-mail addresses: zhnaqshbandi@gmail.com (Z. Naghshbandi), absalimi@uok.ac.ir (A. Salimi).

https://doi.org/10.1016/j.jelechem.2025.119580
Received 26 August 2025; Received in revised form 20 October 2025; Accepted 23 October 2025
Available online 24 October 2025
1572-6657/

Transition metal-based materials, including oxides, sulfides, and polyoxometalates (POMs), have become promising options because of their rich redox chemistry, structural flexibility, and cost-effectiveness. Transition metal sulfides, such as molybdenum sulfides and cobalt sulfides, have been widely studied for electrocatalytic water splitting because of their high activity. Molybdenum disulfide (MoS_2), for example, has a layered structure with a large surface area, but its poor conductivity, limited active sites, and low durability restrict its catalytic performance [21]. To overcome these issues, modified MoS_2-based catalysts have been developed. Wu et al. reported Mo, Co co-doped NiS bulk materials grown on Ni foam (Mo,Co-NiS/NF) as effective electrocatalysts for HER and OER [22]. Similarly, Hou et al. created bimetallic sulfides (CoS_2–MoS_2 and Ni_3S_2–MoS_2 nanoflowers) on carbon cloth, used for HER in acidic solutions [23]. Nickel and cobalt-incorporated MoS_2 nanoboxes (Ni–Co–MoS_2) [24] and Anderson-type polyoxometalates (Co-Mo-S/CC) [25] have also demonstrated promising performance as electrocatalysts for water splitting. Currently, many polyoxometalate/ZIF-derived materials are employed as electrocatalysts for water splitting. The synthesized Mo_xCo_xC@C based on $[PMo_{12}O_{40}]^{3-}$ (PMo_{12}) clusters embedded into uniform ZIF-67 [26], and the Co/Cu-containing polyoxometalate/carbon cloth (Cu_6Co_7/CC) hybrid [27], have been used as efficient electrocatalysts for overall water splitting. These findings emphasize the potential of POM/MOF-based precursors for producing metal-ion-doped materials with enhanced catalytic activity.

Among these, POMs stand out as a diverse class of molecular inorganic compounds made up of metal–oxygen cluster anions. Usually formed from transition metals (TMs) like W, Mo, V, Nb, and Ta with high oxidation states in d_0 or d_1 electronic configurations, these structures are linked by oxygen atoms [28–31]. POMs are highly valued for their excellent redox capacity, thermal stability, and adjustable structures, which make them very versatile for a range of applications such as catalysis, medicine, electrochemistry, and photochromism [32–34]. However, their limited electrical conductivity and the presence of crystal water within their structure significantly hinder their catalytic efficiency, requiring new strategies to improve their performance.

To overcome these limitations, combining POMs with conductive and structurally stable materials, such as Fe and Co, has proven to be an effective strategy [35,36]. In this study, we utilized sulfur doping to improve the catalytic activity of iron-based POMs (Fe-POM-S), as sulfur incorporation can enhance electrical conductivity and introduce additional active sites for catalytic reactions. To further augment the catalytic performance and stability, we integrated zeolitic imidazolate frameworks (ZIF-67), a subclass of metal-organic frameworks (MOFs), with Fe-POM-S. ZIF-67, constructed from Co^{2+} ions and 2-methylimidazolate linkers, offers a large surface area, exceptional stability, and tunable porosity, making it an excellent candidate for electrocatalytic applications [37–39]. By combining ZIF-67 with Fe-POM-S, the synergistic interaction between the two components enhances the availability of active sites, facilitates charge transfer, and improves overall catalytic performance [40–42].

Building upon this synergistic design, nickel foam (NF) was chosen as the substrate due to its high conductivity, large surface area, and structural integrity. NF serves as an excellent platform for catalyst deposition, allowing efficient electron transfer during electrocatalytic reactions [43]. The integration of Fe-POM-S and ZIF-67 onto NF provides a hierarchical structure that ensures robust mechanical stability and uniform active site distribution. Moreover, calcination of the catalyst at 500 °C was employed to further enhance its stability and activity, particularly for HER, by inducing structural optimization and improving the interaction between the components.

Additionally, the urea oxidation reaction (UOR) was explored as an alternative to OER in this study. Urea, a major pollutant in wastewater, offers a lower thermodynamic potential for oxidation compared to OER, significantly reducing the overall energy input for water splitting [44–47]. Furthermore, urea possesses a high gravimetric energy density, making it an attractive candidate for energy storage and conversion applications [48–50]. Coupling UOR with HER not only enables energy-efficient hydrogen production but also facilitates environmental remediation. Building on the pressing need for sustainable and efficient hydrogen production methods, this study presents a novel, cost-effective, and scalable approach to fabricating a multifunctional electrocatalyst: sulfur-doped Fe-polyoxometalate decorated with ZIF-67 on nickel foam (NF/Fe-POM-S/ZIF-67). Through systematic synthesis and characterization, we demonstrate the exceptional performance of this catalyst for OER, HER, and UOR, addressing critical challenges in renewable energy applications.

2. Experimental

2.1. Chemicals

Ammonium heptamolybdate tetrahydrate ($(NH_4)_6Mo_7O_{24}.4H_2O$), Iron(III) nitrate hexahydrate ($Fe(NO_3)_3.6H_2O$), Thioacetamide (C_2H_5NS), Cobalt(II) acetate tetrahydrate $Co(OAc)_2.4H_2O$, 2-Methylimidazolate, potassium hydroxide (KOH), potassium chloride (KCl), platinum carbon (Pt/C), and ruthenium oxide (RuO_2) were purchased from Merck. The reagents and chemicals were of analytical grade and used directly without further purification.

2.2. Instruments and characterization

The morphology and microstructure of the samples were analyzed using field emission scanning electron microscopy (FE-SEM, Tescan MIRA3, Tescan, Czech Republic). Imaging was performed in secondary electron (SE) mode at accelerating voltages ranging from 5 to 20 kV under high-vacuum conditions. Samples were sputter-coated with a thin layer of gold to minimize charging. Transmission electron microscopy (TEM) was carried out using a Philips/FEI EM 208S operated at an accelerating voltage of 100 kV. The ultrathin sections were deposited on copper grids and examined in bright-field mode to study the internal morphology and particle distribution. X-ray photoelectron spectroscopy (XPS) was performed using a BESTEK EA 10 system (BESTEK, Czech Republic) equipped with a monochromatic Al Kα X-ray source (1486.6 eV). Survey and high-resolution spectra were acquired to determine the elemental composition and chemical states of the sample surface. Charge compensation was applied to minimize surface charging, and the analysis was conducted under ultra-high vacuum conditions ($\sim 10^{-8}$ mbar). The crystal structure of the samples was analyzed by X-ray diffraction (XRD) using a Siemens D-500 diffractometer equipped with a Cu Kα radiation source ($\lambda = 1.5406$ Å) operating in Bragg-Brentano geometry. The diffraction patterns were recorded over a 2Θ range of 5°-80°. Electrochemical experiments were conducted on a computer-controlled m-Autolab modular electrochemical system (Eco Chemie, Utrecht, The Netherlands) operated with GPES software (Eco Chemie).

2.3. Synthesis of NF/Fe-POM and NF/Fe-POM-S

A piece of commercial nickel foam (NF) (4×8 cm) was ultrasonically cleaned in water and ethanol to ensure surface cleanliness and enhance wettability. Subsequently, 0.12 mmol of ammonium heptamolybdate tetrahydrate ($(NH_4)_6Mo_7O_{24}.4H_2O$) and 0.72 mmol of iron(III) nitrate hexahydrate ($Fe(NO_3)_3.6H_2O$) were dissolved in 20 mL of deionized water. The pretreated NF was immersed in the solution, which was then refluxed at 100 °C for 15 h with gentle stirring. The resulting product (NF/Fe-POM) was thoroughly washed with deionized water and ethanol to remove unreacted precursors and dried at 60 °C.

To introduce sulfur doping, NF/Fe-POM was immersed in a solution of 1.3 mmol of thioacetamide dissolved in 20 mL of a 1:1 mixture of water and ethanol. The mixture was transferred to a 50 mL Teflon-lined stainless-steel autoclave and heated at 180 °C for 10 h. After cooling to room temperature, the NF/Fe-POM-S was collected, rinsed extensively with deionized water and ethanol, and dried at 60 °C. POM typically has a framework built primarily from Mo—O. Sulfur can substitute for oxygen atoms (Mo—S). Sulfur is less electronegative than oxygen, making Mo centers more electron-rich and enhancing electron transfer rates, lowering the overpotential. In addition, S doping introduces vacancies or distortion in the POM framework and more catalytically active sites [51].

2.4. Synthesis of NF/Fe-POM-S/ZIF-67

To synthesize ZIF-67 on NF/Fe-POM-S, 0.6 mmol of cobalt (II) acetate tetrahydrate ($Co(OAc)_2.4H_2O$) was dissolved in 10 mL of methanol and stirred for 10 min to form a homogeneous cobalt solution. In a separate container, 6 mmol of 2-methylimidazolate was dissolved in 10 mL of methanol to prepare the linker solution. The NF/Fe-POM-S substrate was immersed in the cobalt solution, and the 2-methylimidazolate solution was slowly added dropwise under continuous stirring. The combined mixture was stirred at room temperature for 24 h to facilitate the growth of ZIF-67 on the NF/Fe-POM-S surface. After the reaction, the NF/Fe-POM-S loaded with ZIF-67 (NF/Fe-POM-S/ZIF-67) was retrieved, thoroughly washed with deionized water and ethanol to remove unreacted precursors, and dried at 60 °C. The schematic representation of the synthesis of NF/Fe-POM-S/ZIF-67 is shown in Scheme 1.

2.5. Synthesis of NF/Fe-POM-S/ZIF-67 (500 °C)

To perform the calcination of NF/Fe-POM-S/ZIF-67, 100 mg of the material was placed in a quartz boat and heated in a furnace to 500 °C at a ramp rate of 5 °C min^{-1} for 3 h under a continuous nitrogen flow. After calcination, the furnace was allowed to cool naturally to room temperature, yielding NF/Fe-POM-S/ZIF-67 (500 °C). For comparison, other samples, including NF/Fe-POM-S, Fe-POM-S/ZIF-67, and NF/ZIF-67, were also carbonized under identical conditions.

The schematic representation of the synthesis of NF/Fe-POM-S/ZIF-67 is shown in Scheme 1. NF/Fe-POM-S/ZIF-67 was synthesized through a three-step process. First, Fe-POM was loaded onto the surface of nickel foam (NF) using a refluxing method. Next, the Fe-POM on NF was reacted with thioacetamide via a hydrothermal process to form NF/Fe-POM-S. Finally, ZIF-67 was decorated onto the NF/Fe-POM-S by reacting $Co(OAc)_2·4H_2O$ with 2-methylimidazolate at room temperature, resulting in the formation of NF/Fe-POM-S/ZIF-67.

2.6. Electrochemical measurements

The electrocatalytic activities for water splitting and urea oxidation reaction (UOR) were evaluated using a standard three-electrode system at room temperature in a 1 M KOH electrolyte, with 0.5 M urea for UOR measurements. The nickel foam (NF) was used as the working electrode with an effective area of 0.5 cm^2, while a platinum wire served as the counter electrode, and an Ag/AgCl electrode (3 M KCl) was used as the reference electrode. All potentials measured against the Ag/AgCl electrode were calibrated to the reversible hydrogen electrode (RHE) using the Nernst equation ($E_{RHE} = E_{Ag/AgCl} + 0.059 \times pH + 0.197$). Linear sweep voltammetry (LSV) curves were recorded at a scan rate of 5 mV s^{-1}. Overpotentials (η) were calculated using the formula: $\eta = E_{RHE}-E_{Theoretical}$. where the theoretical RHE potentials for OER, HER, and UOR were 1.23 V, 0 V, and 0.47 V, respectively. The kinetic performance of the catalysts was assessed using the Tafel equation: $\eta = b\log j + a$. where η is the overpotential, b is the Tafel slope, and j is the current density. The electrochemical surface area (ECSA) was estimated from the double-layer capacitance (C_{dl}) values, calculated using the equation: $C_{dl} = I/\nu$, where I represents the current density (mA cm^{-2}), and ν is the scan rate (mV s^{-1}). Electrochemical impedance spectroscopy (EIS) was performed to evaluate the charge transfer resistance of the electrocatalyst, with measurements taken over a frequency range of 0.1 Hz to 10 kHz using a modulation voltage of 250 mV. The experiments were conducted in a 1 M KOH solution with a redox probe comprising a 1 mM $K_3[Fe(CN)_6]/K_4[Fe(CN)_6]$ (1:1) and 0.1 M KCl. The stability of the catalyst for OER, HER, and UOR was assessed by chronoamperometric measurements.

The morphological features of NF/Fe-POM-S, NF/Fe-POM-S/ZIF-67, and NF/Fe-POM-S/ZIF-67 (500 °C) were examined using scanning electron microscopy (SEM) and transmission electron microscopy (TEM). The SEM images (Fig. 1a, b) revealed the uniform distribution of Fe-POM-S with a spherical structure on the NF substrate. The SEM images further demonstrated the formation of uniform rhombic dodecahedral crystals of ZIF-67 on NF/Fe-POM-S (Fig. 1c, d). Upon calcination at 500 °C, the morphology of NF/Fe-POM-S/ZIF-67 remained stable, as evidenced by the consistent rhombic dodecahedral crystal structure observed in SEM images (Fig. 1e, f). This stability indicates the structural robustness of NF/Fe-POM-S/ZIF-67 under thermal treatment. Similarly, TEM images of NF/Fe-POM-S/ZIF-67 (Fig. 1g, h) corroborated the SEM observations, highlighting the preservation of the rhombic dodecahedral morphology.

The uniform distribution of key elements C, N, S, Mo, Fe, Co, and Ni was confirmed through SEM-based elemental mapping (Fig. 1i). The energy-dispersive X-ray (EDX) analysis further quantified the elemental composition of NF/Fe-POM-S/ZIF-67, showing weight percentages of 24.16 % (C), 14.08 % (N), 22.88 % (S), 11.17 % (Mo), 1.52 % (Fe), 1.97 % (Co), and 24.22 % (Ni) (Fig. S1). These results indicate the successful integration of all components into the composite structure.

The phase and crystalline structures of NF, NF/Fe-POM-S, ZIF-67, NF/Fe-POM-S/ZIF-67 and NF/Fe-POM-S/ZIF-67 (500 °C) were analyzed using X-ray diffraction (XRD), as shown in Fig. 2a. The diffraction peaks at 44.7°, 52.02°, and 76.1° correspond to the (111), (200), and (220) crystal planes of NF, respectively. Characteristic peaks of Fe-POM-S were observed at 2Θ values of 9.98°, 26.1°, 26.4°, 31.4°, and 38.1°, which are assigned to the (001), (021), (002), (222), and (003) planes. Additionally, sharp peaks at 7.3°, 10.6°, 12.8°, 15.1°, 16.7°, 18.2°, 24.9°, and 27.3° correspond to the (011), (002), (112), (022), (013), (222), (114), and (233) planes, which are in good agreement with the

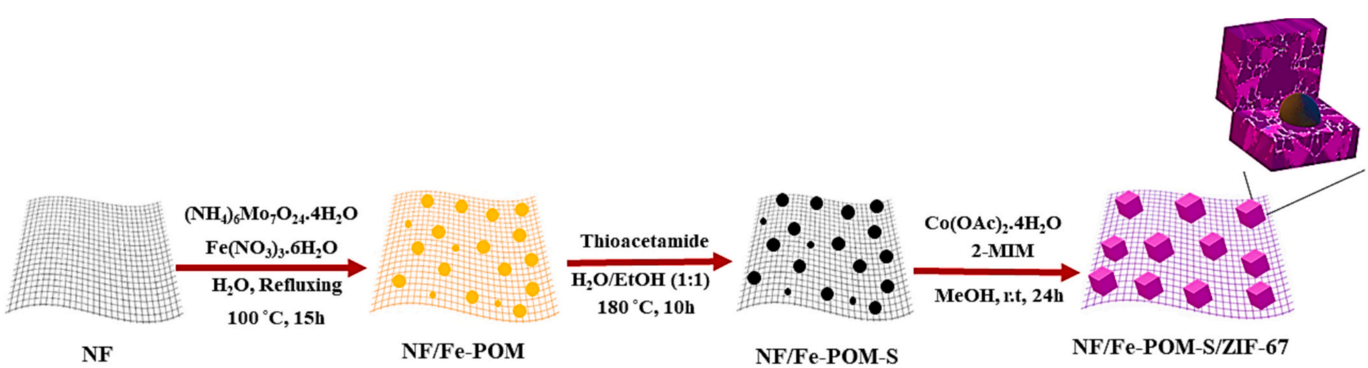

Scheme 1. Schematic illustration of the synthetic process for NF/Fe-POM-S/ZIF-67.

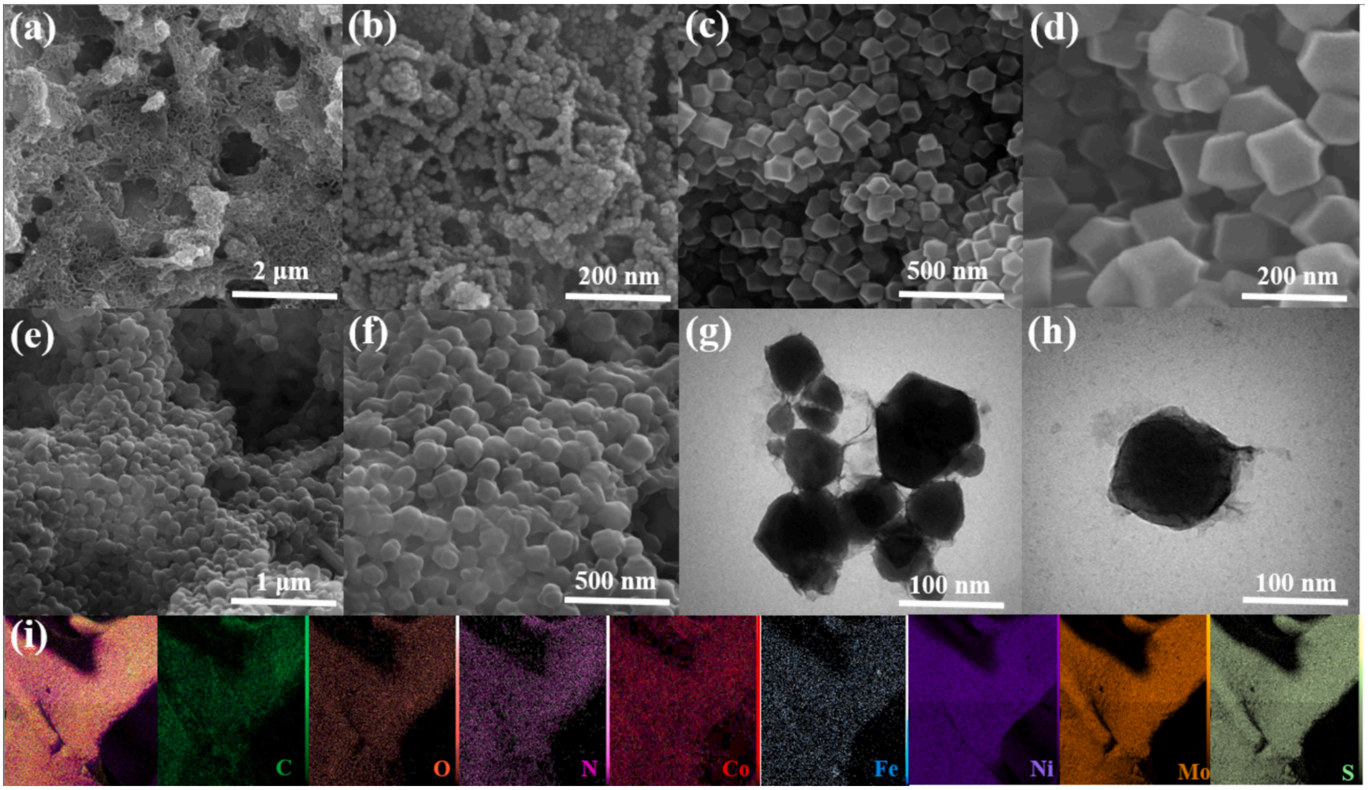

Fig. 1. SEM images of (a, b) NF@Fe-POM-S, (c, d) NF/Fe-POM-S/ZIF-67, and (e, f) NF/Fe-POM-S/ZIF-67 (500 °C), TEM images of (g, h) NF/Fe-POM-S/ZIF-67 and (i) EDS elemental mapping of NF/Fe-POM-S/ZIF-67.

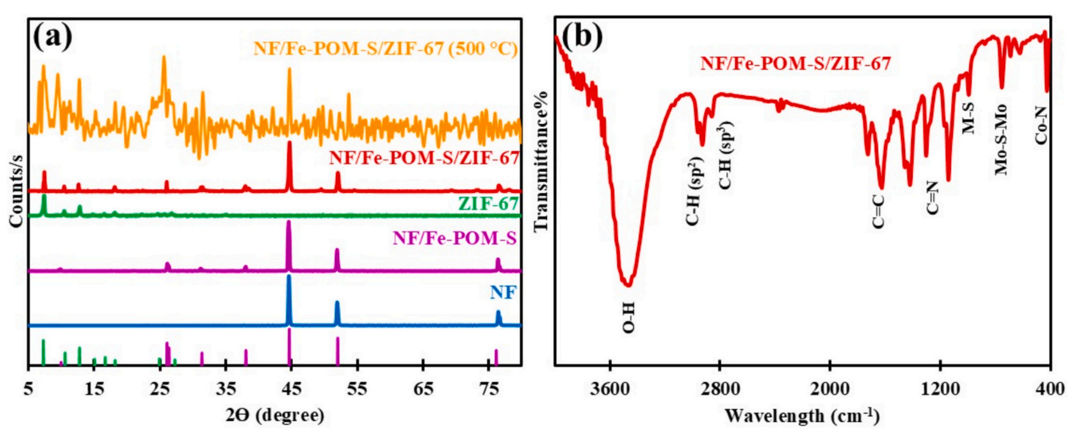

Fig. 2. (a) XRD patterns of NF, NF/Fe-POM-S, ZIF-67, NF/Fe-POM-S/ZIF-67 and NF/Fe-POM-S/ZIF-67 (500 °C), (b) FT-IR spectra of NF/Fe-POM-S/ZIF-67.

crystalline structure of ZIF-67. These XRD results confirm the successful integration of NF, Fe-POM-S, and ZIF-67 components in the composite [48–54]. Moreover, the XRD pattern of NF/Fe-POM-S/ZIF-67 (500 °C) demonstrated that the structure is stable despite calcination at 500 °C.

The formation of NF/Fe-POM-S/ZIF-67 was further validated using Fourier Transform Infrared (FT-IR) spectroscopy, as presented in Fig. 2b. A broad peak at 3425 cm^{-1} was attributed to the stretching vibration of hydroxyl (OH) groups associated with interlayer water molecules. Peaks at 2925 cm^{-1} and 2856 cm^{-1} correspond to the stretching modes of C—H bonds in the aromatic ring and aliphatic chain of 2-methylimidazolate (2-MIM), respectively. The peak at 1622 cm^{-1} is associated with the stretching vibration of the C═C bond, while peaks at 1419 cm^{-1} and 1139 cm^{-1} are indicative of C═N stretching vibrations. Additionally, characteristic peaks at 992 cm^{-1}, 754 cm^{-1}, and 424 cm^{-1} are attributed to the stretching vibrations of M–S (M = Mo and Fe), Mo–S–Mo, and Co—N bonds, respectively [48–54].

X-ray photoelectron spectroscopy (XPS) was also employed to analyze the surface chemical states of elements in NF/Fe-POM-S/ZIF-67 (Fig. 3). The survey spectrum confirmed the coexistence of Ni, Mo, Fe, S, N, C, and Co elements, indicating successful integration of all components. The S 2p spectrum was deconvoluted into two peaks at 161.6 eV and 162.8 eV, corresponding to S $2p_{3/2}$ and S $2p_{1/2}$, respectively, confirming the formation of sulfur-metal bonds [55]. The Mo 3d spectrum displayed binding energy peaks at 231.8 eV (Mo $3d_{5/2}$) and 234.9 eV (Mo $3d_{3/2}$), which are characteristic of a Mo^{6+} oxidation state [56,57]. In the C 1 s spectrum, four distinct peaks were observed at 284.5 eV, 285.4 eV, 286.4 eV, and 287.9 eV, corresponding to C═C, C═N, C—O, and C—N bonds, respectively [58], indicating the presence of functional groups from the ZIF-67 framework and sulfur doping. Similarly, the N 1 s spectrum revealed peaks at 400.4 eV, 401.6 eV, and 402.5 eV, which

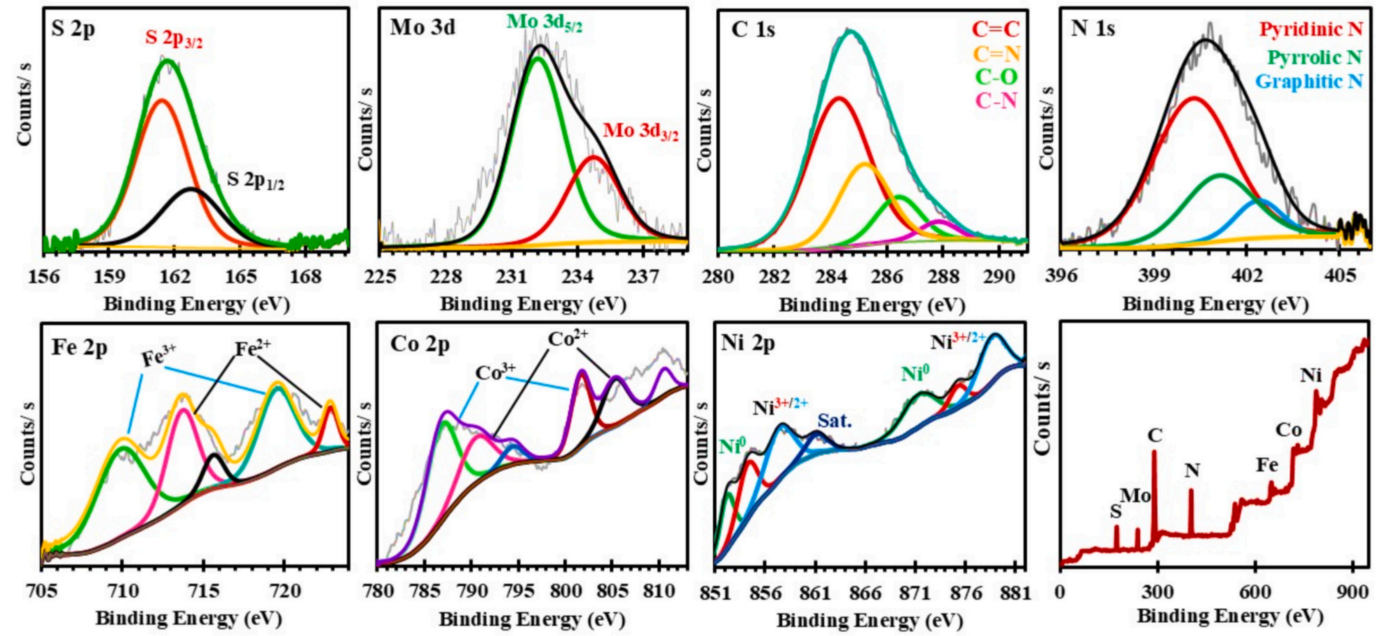

Fig. 3. XPS spectra of NF/Fe-POM-S/ZIF-67: S 2p, Mo 3d, C 1 s, N 1 s, Fe 2p, Co 2p, Ni 2p, and the survey spectrum.

were assigned to pyridinic, pyrrolic, and graphitic nitrogen species, respectively [59,60]. The Fe 2p spectrum exhibited four peaks: 709.3 eV (Fe $2p_{3/2}$) and 719.3 eV (Fe $2p_{1/2}$) corresponded to Fe^{3+}, while 713.1 eV (Fe $2p_{3/2}$) and 723.2 eV (Fe $2p_{1/2}$) were attributed to Fe^{2+} [56,57]. The Co 2p spectrum displayed peaks characteristic of Co^{3+} at 786.3 eV ($2p_{3/2}$) and 802.5 eV ($2p_{1/2}$), as well as peaks for Co^{2+} at 791.6 eV ($2p_{3/2}$) and 806.2 eV ($2p_{1/2}$) [59,60]. Finally, the Ni 2p spectrum displayed peaks at 852.1 eV and 871.2 eV for metallic Ni^0, and the peaks at 854.1, 874.6 eV and 857.1, 878.7 eV were assigned to the $2p_{3/2}$ and $2p_{1/2}$ spin orbital peaks of Ni^{3+} and Ni^{2+}, respectively [61–63]. These XPS results demonstrate significant electronic interactions between the Ni foam substrate, Fe-POM-S, and ZIF-67, which play a crucial role in enhancing the electrocatalytic performance of the composite.

The electrocatalytic activities of the synthesized samples were

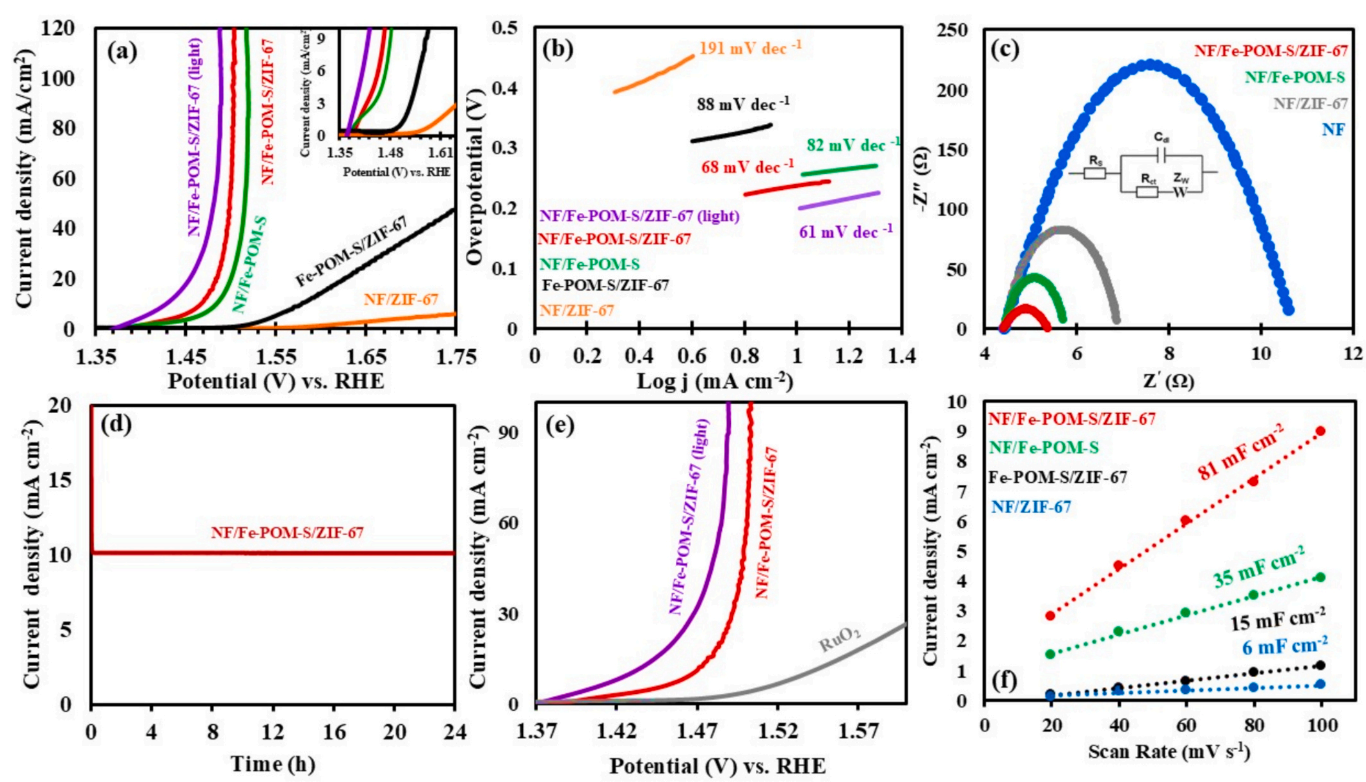

Fig. 4. Electrocatalytic performance of the as-prepared catalysts for OER: (a) OER polarization curves, (b) Tafel slopes for OER, (c) Electrochemical impedance spectroscopy (EIS), (d) Long-term stability test of NF/Fe-POM-S/ZIF-67, (e) Comparison of OER polarization curves for NF/Fe-POM-S/ZIF-67 (light-irradiated), NF/Fe-POM-S/ZIF-67 (ambient conditions), and RuO_2 (f) Double-layer capacitance (C_{dl}) of the as-prepared electrocatalysts.

evaluated for the oxygen evolution reaction (OER) and hydrogen evolution reaction (HER) using a three-electrode system in 1.0 M KOH. Linear sweep voltammetry (LSV) was performed at a scan rate of 5 mV s^{-1}, with manual 90 % iR-correction applied to all data using electrochemical impedance spectroscopy (EIS). As shown in Fig. 4a, the OER performance of NF/Fe-POM-S/ZIF-67, NF/Fe-POM-S, Fe-POM-S/ZIF-67, and NF/ZIF-67 was assessed under both light irradiation and ambient conditions. NF/Fe-POM-S/ZIF-67 under light irradiation exhibited superior performance with a lower onset potential of 1.39 V compared to 1.42 V under ambient conditions. The overpotential (η) for NF/Fe-POM-S/ZIF-67 (light), NF/Fe-POM-S/ZIF-67, NF/Fe-POM-S, Fe-POM-S/ZIF-67, and NF/ZIF-67 was calculated as 190, 230, 260, 350, and 420 mV, respectively, at a current density of 10 mA cm^{-2}. NF/Fe-POM-S/ZIF-67 (light) and NF/Fe-POM-S/ZIF-67 also demonstrated better performance than RuO_2 (Fig. 4e), highlighting the synergistic effects of NF, Fe-POM-S, and ZIF-67.

The Tafel slopes for OER (Fig. 4b) confirmed faster reaction kinetics for NF/Fe-POM-S/ZIF-67 under light irradiation, which showed the lowest Tafel slope of 61 mV dec^{-1}. NF/Fe-POM-S/ZIF-67, NF/Fe-POM-S, Fe-POM-S/ZIF-67, and NF/ZIF-67 exhibited Tafel slopes of 68, 82, 88, and 191 mV dec^{-1}, respectively, indicating the superior catalytic kinetics of NF/Fe-POM-S/ZIF-67. EIS analysis (Fig. 4c) revealed that NF/Fe-POM-S/ZIF-67 exhibited the lowest charge transfer resistance (R_{ct}) of 0.9 Ω, compared to 1.4 Ω for NF/Fe-POM-S, 2.6 Ω for Fe-POM-S/ZIF-67, and 6.6 Ω for NF/ZIF-67. The low R_{ct}, evaluated by EIS at a set potential of 1.5 V, facilitated faster charge transfer and enhanced catalytic activity.

The long-term electrochemical stability of NF/Fe-POM-S/ZIF-67 for OER was evaluated using chronoamperometric analysis in 1.0 M KOH at 1.5 V (Fig. 4d). The current density remained stable over 24 h, demonstrating excellent long-term stability. Additionally, a Long-term stability test at a higher current density of 100 mA cm^{-2} was performed in 48 h, and the result showed that 95 % of the NF/Fe-POM-S/ZIF-67 remained after 48 h (Fig. S2). Post-stability analysis using SEM (Fig. S4) and XRD (Fig. S5) confirmed that the morphology and structure of NF/Fe-POM-S/ZIF-67 remained intact.

The electrochemically active surface area (ECSA) was determined from the double-layer capacitance (C_{dl}) values obtained via cyclic voltammetry in the non-faradaic region (Fig. S3) and (Fig. 4f) [64]. NF/Fe-POM-S/ZIF-67 exhibited the highest C_{dl} value of 81 mF cm^{-2}, significantly greater than NF/Fe-POM-S (35 mF cm^{-2}), Fe-POM-S/ZIF-67 (15 mF cm^{-2}), and NF/ZIF-67 (6 mF cm^{-2}), indicating a higher density of catalytically active sites.

POMs act as photosensitizers, absorbing visible or UV light due to their strong d–d or LMCT transitions. Upon light absorption, photoexcited electrons are promoted from HOMO to LUMO. Electrons from excited POMs can be transferred to ZIF-67. ZIF-67 can act as conductive pathways or co-catalysts, helping separate and transport charges. This suppresses charge recombination and facilitates hole accumulation for oxidation. The photo-generated holes (h^+) on POMs or metal centers in ZIF can oxidize water molecules [65,66].

HER performance was evaluated for NF/Fe-POM-S/ZIF-67 (500 °C), NF/Fe-POM-S (500 °C), Fe-POM-S/ZIF-67 (500 °C), and NF/ZIF-67 (500 °C) using LSV (Fig. 5a). NF/Fe-POM-S/ZIF-67 (500 °C) demonstrated superior HER activity with an overpotential of 110 mV at 10 mA cm^{-2}, outperforming NF/Fe-POM-S (170 mV), Fe-POM-S/ZIF-67 (273 mV), and NF/ZIF-67 (339 mV). The enhanced performance is attributed to the synergistic effects of the NF, Fe-POM-S, and ZIF-67 components, further optimized by calcination. Tafel slopes (Fig. 5b) confirmed this observation, with NF/Fe-POM-S/ZIF-67 (500 °C) exhibiting the lowest Tafel slope of 95 mV dec^{-1}, compared to 182 mV dec^{-1} for NF/Fe-POM-S, 121 mV dec^{-1} for Fe-POM-S/ZIF-67, and 270 mV dec^{-1} for NF/ZIF-67. To investigate the catalytic kinetic characteristics of the NF/Fe-POM-S/ZIF-67 (500 °C) during HER electrochemical impedance spectroscopy (EIS) was performed over a frequency range of 0.1 Hz to 10 kHz in 1.0 M KOH (Fig. 5c). The transfer resistance (R_{ct}) of NF/Fe-POM-S/ZIF-67 (500 °C) was measured 2.6 Ω, which is lower than NF/Fe-POM-S (500 °C) (5.9 Ω), NF/ ZIF-67 (500 °C) (15.71 Ω), and NF (500 °C) (28.8 Ω). Chronopotentiometric analysis (Fig. 5d) confirmed the stability of NF/Fe-POM-S/ZIF-67 (500 °C) for HER, with negligible

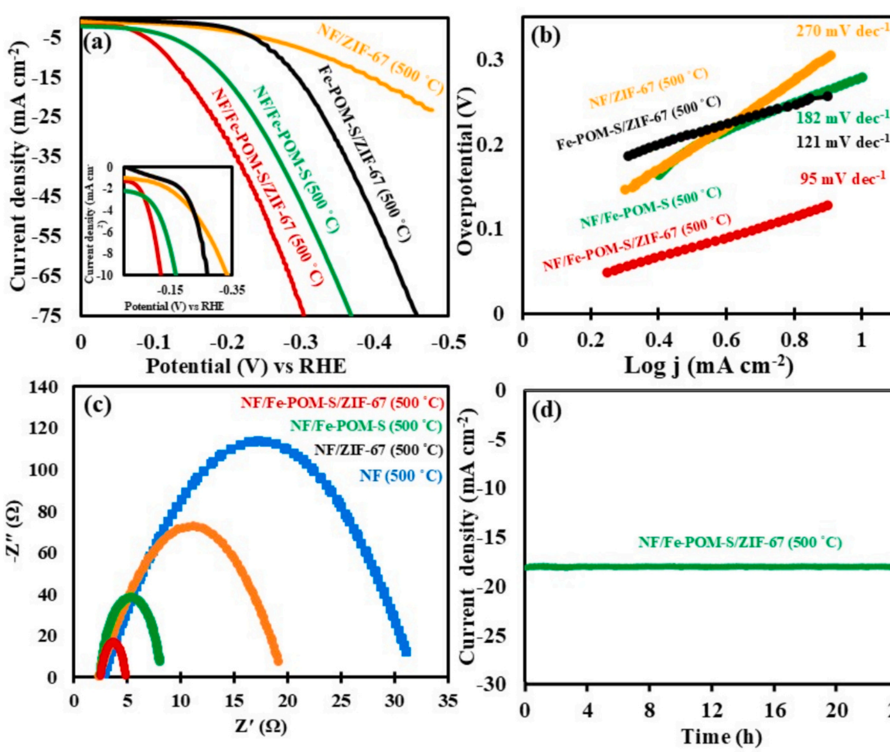

Fig. 5. Electrocatalytic performance of the as-prepared catalysts for HER: (a) HER polarization curves, (b) Tafel slopes for HER, (c) Electrochemical impedance spectroscopy (EIS), (d) Long-term stability test of NF/Fe-POM-S/ZIF-67 (500 °C).

performance degradation over 24 h at a stable potential of 1.5 V in 1.0 M KOH.

To demonstrate practical applicability, NF/Fe-POM-S/ZIF-67 under light illumination and NF/Fe-POM-S/ZIF-67 (500 °C) were employed as the anode and cathode, respectively, in a two-electrode electrolyzer for overall water splitting in 1.0 M KOH (Fig. 6a). This electrolyzer achieved a current density of 10 mA cm^{-2} with a low cell voltage of 1.5 V, outperforming a Pt/C|| RuO_2 as cathode and anode for water splitting. As illustrated for Pt/C|| RuO_2 cell for a current density of 10 mA cm^{-2} the cell voltage was 1.73 V under identical conditions. Long-term stability was confirmed via LSV after 1000 cyclic voltammetry (CV) cycles (Fig. 6b), with minimal changes observed, further highlighting the robustness of the NF/Fe-POM-S/ZIF-67||NF/Fe-POM-S/ZIF-67 (500 °C) system.

2.7. Urea oxidation reaction (UOR)

The UOR catalytic activity of NF/Fe-POM-S/ZIF-67 was evaluated using LSV at a scan rate of 5 mV s^{-1} in an electrolyte containing 0.5 M urea and 1.0 M KOH (Fig. 7a). NF/Fe-POM-S/ZIF-67 exhibited superior UOR catalytic activity compared to other samples and commercial RuO_2. At a current density of 10 mA cm^{-2}, NF/Fe-POM-S/ZIF-67 required a potential of 1.33 V, significantly lower than NF/Fe-POM-S (1.36 V), Fe-POM-S/ZIF-67 (1.38 V), and NF/ZIF-67 (1.43 V). Additionally, the long-term stability of NF/Fe-POM-S/ZIF-67 was assessed using chronopotentiometry at a constant potential of 1.4 V in 1.0 M KOH for 24 h (Fig. 7b). The results demonstrated excellent electrochemical durability, with negligible performance degradation. The Tafel slope of NF/Fe-POM-S/ZIF-67 was measured to be 40 mV dec^{-1}, substantially lower than NF/Fe-POM-S (105 mV dec^{-1}), Fe-POM-S/ZIF-67 (110 mV dec^{-1}), and NF/ZIF-67 (122 mV dec^{-1}) (Fig. 7c). The smaller Tafel slope of NF/Fe-POM-S/ZIF-67 highlights its faster reaction kinetics and superior catalytic efficiency.

To further investigate its performance in overall urea electrolysis, a two-electrode electrolyzer was assembled using NF/Fe-POM-S/ZIF-67 as the anode and NF/Fe-POM-S/ZIF-67 (500 °C) as the cathode. LSV plots revealed that the electrolyzer achieved a current density of 10 mA cm^{-2} at a cell voltage of 1.38 V, outperforming the Pt/C||RuO_2 electrolyzer under identical conditions. Stability was confirmed by comparing LSV curves before and after 1000 cyclic voltammetry (CV) cycles. The post-1000-cycle LSV showed only a slight potential increase of 10 mV, with a potential of 1.39 V at 10 mA cm^{-2}, demonstrating excellent long-term durability of the NF/Fe-POM-S/ZIF-67||NF/Fe-POM-S/ZIF-67 (500 °C) electrolyzer (Fig. 7d).

2.8. Potential mechanism for the OER, HER and UOR on NF/Fe-POM-S/ZIF-67

The NF/Fe-POM-S/ZIF-67 catalyst exhibits excellent electrocatalytic performance in alkaline media. Nickel foam (NF) provides a conductive scaffold, ensuring efficient electron transport and structural stability. While the polyoxometalate (POM) containing Fe and Mo, doped with sulfur, serves as the primary catalytic center: Fe sites facilitate water oxidation, Mo enhances electronic conductivity, and sulfur modifies the electronic structure to promote OH^- adsorption and activation. ZIF-67 deposited on the POM surface increases the accessible surface area and provides Co active sites, which can form CoOOH species under alkaline conditions. Under light irradiation, ZIF-67 generates photoexcited electrons that are efficiently transferred through the POM to the NF, enhancing charge separation and accelerating the OER kinetics. OH^- ions adsorbed on the Fe/Mo/S and Co sites undergo oxidation, producing O_2 with improved efficiency. Calcination of the NF/Fe-POM-S/ZIF-67 catalyst at 500 °C significantly enhances HER performance. The high-temperature treatment improves electronic conductivity by removing organic ligands and forming a more crystalline and stable metal/oxide phase. Additionally, calcination increases the accessible surface area and preserves a porous structure, providing more active sites for water reduction. These structural and electronic improvements also enhance the catalyst's stability under alkaline conditions, resulting in faster HER kinetics and superior long-term performance. Stepwise urea oxidation occurring at Fe/Mo/S and Co active sites. The synergistic integration of NF, POM-S-FeMo, and ZIF-67 ensures high surface area, rapid electron transfer, and superior catalytic performance OER, HER and UOR.

To benchmark the catalytic performance, the OER and HER activities in 1.0 M KOH [67–75], as well as UOR activity in 0.5 M urea with 1.0 M KOH [76–82], and overall water splitting performance in 1.0 M KOH [68,72,83–87], of NF/Fe-POM-S/ZIF-67 at 10 mA cm^{-2} were compared to some other previously reported electrocatalysts (Fig. 8). The results highlight that the synergistic heterostructure of NF, Fe-POM-S, and ZIF-67 provided rich active sites and facilitated effective charge transfer, resulting in superior electrocatalytic performance compared to similar catalysts. Furthermore, the low cost, high efficiency, and long-term stability of these catalysts encourage their design and exploration for water-splitting applications over a wide pH range.

In summary, NF/Fe-POM-S/ZIF-67 was successfully synthesized through the stepwise growth of sulfur-doped iron polyoxometalate (Fe-POM-S) on nickel foam (NF), followed by the decoration of ZIF-67. The composite demonstrated outstanding electrocatalytic performance for the oxygen evolution reaction (OER), hydrogen evolution reaction

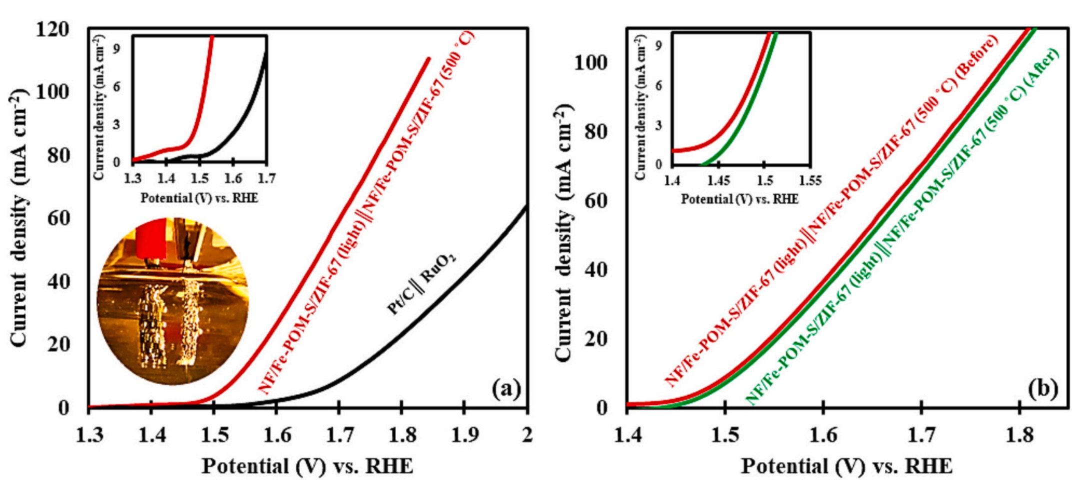

Fig. 6. (a) Polarization curves of NF/Fe-POM-S/ZIF-67 || NF/Fe-POM-S/ZIF-67 (500 °C) compared to Pt/C‖RuO_2, (b) Stability of NF/Fe-POM-S/ZIF-67 || NF/Fe-POM-S/ZIF-67 (500 °C) using LSV before and after 1000 CV cycles.

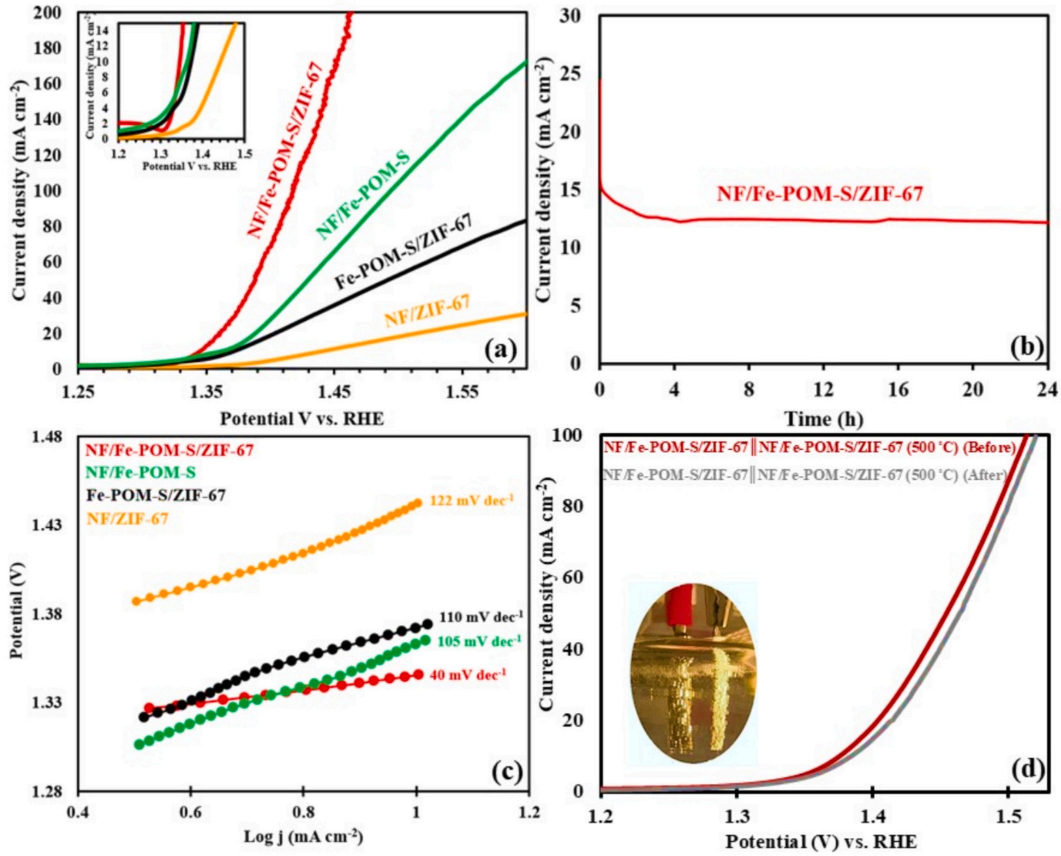

Fig. 7. UOR electrocatalytic performance of the as-prepared samples: (a) LSV curves for UOR, (b) Electrochemical stability test of NF/Fe-POM-S/ZIF-67, (c) Tafel slope plot of the synthesized catalysts, and (d) Polarization curves and LSV before and after 1000 CV cycles for the NF/Fe-POM-S/ZIF-67 || NF/Fe-POM-S/ZIF-67 (500 °C) electrolyzer.

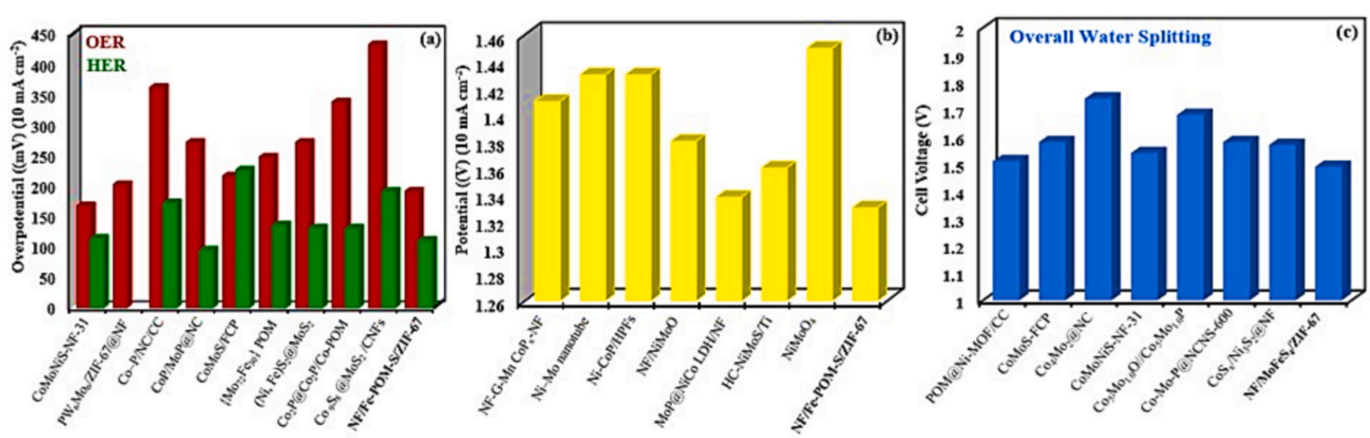

Fig. 8. Comparative performance of NF/Fe-POM-S/ZIF-67 with reported electrocatalysts: (a) OER and HER in 1.0 M KOH, (b) UOR in 1.0 M KOH with 0.5 M urea, and (c) overall water splitting in 1.0 M KOH.

(HER), and urea oxidation reaction (UOR). Under light irradiation, NF/Fe-POM-S/ZIF-67 achieved an overpotential of 190 mV at a current density of 10 mA cm^{-2} for OER, with a Tafel slope of 61 mV dec^{-1}. After calcination at 500 °C, it exhibited an overpotential of 110 mV and a Tafel slope of 95 mV dec^{-1} for HER in 1.0 M KOH. For overall water splitting, an electrolyzer using NF/Fe-POM-S/ZIF-67 as the anode and NF/Fe-POM-S/ZIF-67 (500 °C) as the cathode achieved a cell voltage of 1.5 V at 10 mA cm^{-2} in alkaline media. Additionally, NF/Fe-POM-S/ZIF-67 showed superior UOR activity, requiring only 1.33 V to achieve 10 mA cm^{-2} in an electrolyte containing 0.5 M urea and 1.0 M KOH, while the same electrolyzer achieved a cell voltage of 1.38 V for overall urea electrolysis at 10 mA cm^{-2}. The composite and its calcined counterpart exhibited excellent stability across all three reactions, maintaining performance over prolonged durations. These results underscore the synergistic integration of NF, Fe-POM-S, and ZIF-67, providing a low-cost, high-efficiency, and durable electrocatalyst suitable for water splitting and urea electrolysis applications over a wide pH range, offering valuable insights for the development of next-generation energy systems.

CRediT authorship contribution statement

Zhwan Naghshbandi: Writing – review & editing, Writing – original draft, Data curation. **Abdollah Salimi:** Writing – review & editing, Supervision. **Ali Feizabadi:** Writing – review & editing.

Declaration of competing interest

The authors declare that they have no known competing financial interests or personal relationships that could have appeared to influence the work reported in this paper.

Acknowledgment

Dr. Zhwan Naghshbandi thanks the Research Office of the University of Kurdistan for supporting her Post Doc program (grant number 02–9–33,926-135).

Appendix A. Supplementary data

Supplementary data to this article can be found online at https://doi.org/10.1016/j.jelechem.2025.119580.

References

[1] H. Sun, X. Xu, H. Kim, W. Jung, W. Zhou, Z. Shao, Electrochemical water splitting: bridging the gaps between fundamental research and industrial applications, Energy Environ. Mater. 6 (5) (2023) e12441.
[2] H. Sun, X. Xu, Y. Song, W. Zhou, Z. Shao, Designing high-valence metal sites for electrochemical water splitting, Adv. Funct. Mater. 31 (16) (2021) 2009779.
[3] X. Li, X. Hao, A. Abudula, G. Guan, Nanostructured catalysts for electrochemical water splitting: current state and prospects, J Mater Chem A 4 (31) (2016) 11973–12000.
[4] S. Li, E. Li, X. An, X. Hao, Z. Jiang, G. Guan, Transition metal-based catalysts for electrochemical water splitting at high current density: current status and perspectives, Nanoscale 13 (30) (2021) 12788–12817.
[5] Y. Yan, B.Y. Xia, B. Zhao, X. Wang, A review on noble-metal-free bifunctional heterogeneous catalysts for overall electrochemical water splitting, J Mater Chem A 4 (45) (2016) 17587–17603.
[6] R. Solanki, I. Patra, N. Ahmad, N.B. Kumar, R.M.R. Parra, M. Zaidi, G. Yasin, T.C. A. Kumar, H.A. Hussein, R. Sivaraman, Investigation of recent progress in metal-based materials as catalysts toward electrochemical water splitting, J. Environ. Chem. Eng. 10 (4) (2022) 108207.
[7] D.-D. Qin, Y. Tang, G. Ma, L. Qin, C.-L. Tao, X. Zhang, Z. Tang, Molecular metal nanoclusters for ORR, HER and OER: achievements, opportunities and challenges, Int. J. Hydrog. Energy 46 (51) (2021) 25771–25781.
[8] S. Anantharaj, S. Noda, Amorphous catalysts and electrochemical water splitting: an untold story of harmony, Small 16 (2) (2020) 1905779.
[9] J. Wang, X. Yue, Y. Yang, S. Sirisomboonchai, P. Wang, X. Ma, A. Abudula, G. Guan, Earth-abundant transition-metal-based bifunctional catalysts for overall electrochemical water splitting: a review, J. Alloys Compd. 819 (2020) 153346.
[10] K. Takanabe, Photocatalytic water splitting: quantitative approaches toward photocatalyst by design, ACS Catal. 7 (11) (2017) 8006–8022.
[11] Y.-F. Li, Z.-P. Liu, L. Liu, W. Gao, Mechanism and activity of photocatalytic oxygen evolution on titania anatase in aqueous surroundings, JACS 132 (37) (2010) 13008–13015.
[12] G. Paille, M. Gomez-Mingot, C. Roch-Marchal, M. Haouas, Y. Benseghir, T. Pino, M.-H. Ha-Thi, G. Landrot, P. Mialane, M. Fontecave, Thin films of fully noble metal-free POM@ MOF for photocatalytic water oxidation, ACS Appl. Mater. Interfaces 11 (51) (2019) 47837–47845.
[13] D. Cardenas-Morcoso, R. Ifraemov, M. García-Tecedor, I. Liberman, S. Gimenez, I. Hod, A metal–organic framework converted catalyst that boosts photo-electrochemical water splitting, J Mater Chem A 7 (18) (2019) 11143–11149.
[14] M. Ali, E. Pervaiz, T. Noor, O. Rabi, R. Zahra, M. Yang, Recent advancements in MOF-based catalysts for applications in electrochemical and photoelectrochemical water splitting: a review, Int. J. Energy Res. 45 (2) (2021) 1190–1226.
[15] N. Afzali, R. Keshavarzi, S. Tangestaninejad, S. Gimenez, V. Mirkhani, M. Moghadam, I. Mohammadpoor-Baltork, Multifunctional approach to improve water oxidation performance with MOF-based photoelectrodes, Appl. Mater. Today 24 (2021) 101159.
[16] R. Zhang, J. Sun, Y. Chen, Q. Shen, C. Ding, S. Zhang, J. Zhang, Advanced porous platinum group metal nano-structural electrocatalysts for water electrolysis, fuel cells and metal-air batteries, Coord. Chem. Rev. 543 (2025) 216958.
[17] J. Ni, Z. Shi, Y. Wang, J. Yang, H. Wu, P. Wang, M. Xiao, C. Liu, W. Xing, Development of noble metal-free electrocatalysts towards acidic water oxidation: from fundamental understanding to state-of-the-art catalysts, EScience 5 (2025) 100295.
[18] Z. Tao, T. Wang, X. Wang, J. Zheng, X. Li, MOF-derived noble metal free catalysts for electrochemical water splitting, ACS Appl. Mater. Interfaces 8 (51) (2016) 35390–35397.
[19] S. Anantharaj, S.R. Ede, K. Sakthikumar, K. Karthick, S. Mishra, S. Kundu, Recent trends and perspectives in electrochemical water splitting with an emphasis on sulfide, selenide, and phosphide catalysts of Fe, Co, and Ni: a review, ACS Catal. 6 (12) (2016) 8069–8097.
[20] J. Wang, W. Cui, Q. Liu, Z. Xing, A.M. Asiri, X. Sun, Recent progress in cobalt-based heterogeneous catalysts for electrochemical water splitting, Adv. Mater. 28 (2) (2016) 215–230.
[21] Z.-H. Wang, X.-F. Wang, Z. Tan, X.-Z. Song, Polyoxometalate/metal–organic framework hybrids and their derivatives for hydrogen and oxygen evolution electrocatalysis, Mater. Today Energy 19 (2021) 100618.
[22] C. Wu, Y. Du, Y. Fu, D. Feng, H. Li, Z. Xiao, Y. Liu, Y. Yang, L. Wang, Mo, co co-doped NiS bulks supported on Ni foam as an efficient electrocatalyst for overall water splitting in alkaline media, Sustain. Energy Fuels 4 (4) (2020) 1654–1664.
[23] Y. Hou, H. Pang, L. Zhang, B. Li, J. Xin, K. Li, H. Ma, X. Wang, L. Tan, Highly dispersive bimetallic sulfides afforded by crystalline polyoxometalate-based coordination polymer precursors for efficient hydrogen evolution reaction, J. Power Sources 446 (2020) 227319.
[24] X.-Y. Yu, Y. Feng, Y. Jeon, B. Guan, X.W. Lou, U. Paik, Formation of Ni-co-MoS_2 Nanoboxes with enhanced electrocatalytic activity for hydrogen evolution, Adv. Mater. 28 (40) (2016) 9006–9011.
[25] Y.-J. Tang, A.-M. Zhang, H.-J. Zhu, L.-Z. Dong, X.-L. Wang, S.-L. Li, M. Han, X.-X. Xu, Y.-Q. Lan, Polyoxometalate precursors for precisely controlled synthesis of bimetallic sulfide heterostructure through nucleation-doping competition, Nanoscale 10 (18) (2018) 8404–8412.
[26] C. Chen, A. Wu, H. Yan, Y. Xiao, C. Tian, H. Fu, Trapping $[PMo_{12}O_{40}]$ 3− clusters into pre-synthesized ZIF-67 toward Mo_xCo_xC particles confined in uniform carbon polyhedrons for efficient overall water splitting, Chem. Sci. 9 (21) (2018) 4746–4755.
[27] M. Wang, W. Zhong, S. Zhang, R. Liu, J. Xing, G. Zhang, An overall water-splitting polyoxometalate catalyst for the electromicrobial conversion of CO 2 in neutral water, J.Mater. Chem, A 6 (21) (2018) 9915–9921.
[28] S.-S. Wang, G.-Y. Yang, Recent advances in polyoxometalate-catalyzed reactions, Chem. Rev. 115 (11) (2015) 4893–4962.
[29] M.R. Horn, A. Singh, S. Alomari, S. Goberna-Ferrón, R. Benages-Vilau, N. Chodankar, N. Motta, K.K. Ostrikov, J. MacLeod, P. Sonar, Polyoxometalates (POMs): from electroactive clusters to energy materials, Energy Environ. Sci. 14 (4) (2021) 1652–1700.
[30] X. López, J.J. Carbó, C. Bo, J.M. Poblet, Structure, properties and reactivity of polyoxometalates: a theoretical perspective, Chem. Soc. Rev. 41 (22) (2012) 7537–7571.
[31] N.I. Gumerova, A. Rompel, Synthesis, structures and applications of electron-rich polyoxometalates, Nat. Rev. Chem. 2 (2) (2018) 0112.
[32] Y. Wang, I.A. Weinstock, Polyoxometalate-decorated nanoparticles, Chem. Soc. Rev. 41 (22) (2012) 7479–7496.
[33] J.-X. Liu, X.-B. Zhang, Y.-L. Li, S.-L. Huang, G.-Y. Yang, Polyoxometalate functionalized architectures, Coord. Chem. Rev. 414 (2020) 213260.
[34] D. Li, P. Ma, J. Niu, J. Wang, Recent advances in transition-metal-containing Keggin-type polyoxometalate-based coordination polymers, Coord. Chem. Rev. 392 (2019) 49–80.
[35] M.T. Pope, A. Müller, Polyoxometalate chemistry: an old field with new dimensions in several disciplines, Angew. Chem. Int. Ed. Eng. 30 (1) (1991) 34–48.
[36] B. Chen, Z. Yang, Y. Zhu, Y. Xia, Zeolitic imidazolate framework materials: recent progress in synthesis and applications, J Mater Chem A 2 (40) (2014) 16811–16831.
[37] J. Yao, H. Wang, Zeolitic imidazolate framework composite membranes and thin films: synthesis and applications, Chem. Soc. Rev. 43 (13) (2014) 4470–4493.
[38] J. Li, R. Ge, Y. Li, R. Zheng, J. Yang, J. Zhang, M. Zhu, S. Li, J. Feng, B. Liu, Zeolitic imidazolate framework-67 derived cobalt-based catalysts for water splitting, Mater. Today Chem. 26 (2022) 101210.
[39] H. Wen, S. Zhang, T. Yu, Z. Yi, R. Guo, ZIF-67-based catalysts for oxygen evolution reaction, Nanoscale 13 (28) (2021) 12058–12087.
[40] G. Zhong, D. Liu, J. Zhang, The application of ZIF-67 and its derivatives: adsorption, separation, electrochemistry and catalysts, J Mater Chem A 6 (5) (2018) 1887–1899.
[41] S. Bibi, E. Pervaiz, M. Ali, Synthesis and applications of metal oxide derivatives of ZIF-67: a mini-review, Chem. Pap. 75 (2021) 2253–2275.
[42] M. Ali, E. Pervaiz, T. Noor, O. Rabi, R. Zahra, M. Yang, Recent advancements in MOF-based catalysts for applications in electrochemical and photoelectrochemical water splitting: a review, Int. J. Energy Res. 45 (2) (2021) 1190–1226.
[43] N.K. Chaudhari, H. Jin, B. Kim, K. Lee, Nanostructured materials on 3D nickel foam as electrocatalysts for water splitting, Nanoscale 9 (34) (2017) 12231–12247.
[44] W. Ge, L. Lin, S.-Q. Wang, Y. Wang, X. Ma, Q. An, L. Zhao, Electrocatalytic urea oxidation: advances in mechanistic insights, nanocatalyst design, and applications, J Mater Chem A 11 (28) (2023) 15100–15121.
[45] X. Gao, S. Zhang, P. Wang, M. Jaroniec, Y. Zheng, S.-Z. Qiao, Urea catalytic oxidation for energy and environmental applications, Chem. Soc. Rev. 53 (2024) 1552.
[46] G. Gnana Kumar, A. Farithkhan, A. Manthiram, Direct urea fuel cells: recent progress and critical challenges of urea oxidation electrocatalysis, Adv. Energ. Sust. Res. 1 (1) (2020) 2000015.
[47] B. Zhu, Z. Liang, R. Zou, Designing advanced catalysts for energy conversion based on urea oxidation reaction, Small 16 (7) (2020) 1906133.

[48] W. Sun, J. Li, W. Gao, L. Kang, F. Lei, J. Xie, Recent advances in the pre-oxidation process in electrocatalytic urea oxidation reactions, Chem. Commun. 58 (15) (2022) 2430–2442.
[49] K.S. Anuratha, M. Rinawati, T.-H. Wu, M.-H. Yeh, J.-Y. Lin, Recent development of nickel-based electrocatalysts for urea electrolysis in alkaline solution, Nanomaterials 12 (17) (2022) 2970.
[50] E.T. Sayed, M.A. Abdelkareem, A. Bahaa, T. Eisa, H. Alawadhi, S. Al-Asheh, K.-J. Chae, A. Olabi, Synthesis and performance evaluation of various metal chalcogenides as active anodes for direct urea fuel cells, Renew. Sust. Energ. Rev. 150 (2021) 111470.
[51] J. Gautam, Y. Liu, J. Gu, Z. Ma, J. Zha, B. Dahal, L.N. Zhang, A.N. Chishti, L. Ni, G. Diao, Fabrication of polyoxometalate anchored zinc cobalt sulfide nanowires as a remarkable bifunctional electrocatalyst for overall water splitting, Adv. Funct. Mater. 31 (2021) 2106147.
[52] L. Zhang, T. Mi, M.A. Ziaee, L. Liang, R. Wang, Hollow POM@ MOF hybrid-derived porous $Co_3O_4/CoMoO_4$ nanocages for enhanced electrocatalytic water oxidation, J Mater Chem A 6 (4) (2018) 1639–1647.
[53] K. Lu, T. Gu, L. Zhang, Z. Wu, R. Wang, X. Li, POM-assisted coating of MOF-derived Mo-doped Co_3O_4 nanoparticles on carbon nanotubes for upgrading oxygen evolution reaction, Chem. Eng. J. 408 (2021) 127352.
[54] E.S. Behbahani, K. Dashtian, M. Ghaedi, Fe_3O_4-$FeMoS_4$: promise magnetite LDH-based adsorbent for simultaneous removal of pb (II), cd (II), and cu (II) heavy metal ions, J. Hazard. Mater. 410 (2021) 124560.
[55] X. Han, K. Tao, D. Wang, L. Han, Design of a porous cobalt sulfide nanosheet array on Ni foam from zeolitic imidazolate frameworks as an advanced electrode for supercapacitors, Nanoscale 10 (6) (2018) 2735–2741.
[56] K. Krishnamoorthy, P. Pazhamalai, R. Swaminathan, V. Mohan, S.J. Kim, Unravelling the bi-functional electrocatalytic properties of $\{mo_{72}fe_{30}\}$ polyoxometalate nanostructures for overall water splitting using scanning electrochemical microscope and electrochemical gating methods, Adv. Sci. 2401073 (2024).
[57] Z. Zhang, W. Li, T.-W. Ng, W. Kang, C.-S. Lee, W. Zhang, Iron (II) molybdate ($FeMoO_4$) nanorods as a high-performance anode for lithium ion batteries: structural and chemical evolution upon cycling, J Mater Chem A 3 (41) (2015) 20527–20534.
[58] C.-Y. Wang, C.-Z. Ren, K.-M. Fang, J.-J. Feng, Y. Shi, Y.-J. Gao, A.-J. Wang, Synergistic catalysis of satellite single-atomic Fe sites and RuFe nanoclusters on N-rich carbon nanoflowers for boosting oxygen reduction, J. Colloid Interface Sci. 138169 (2025).
[59] Z. Naghshbandi, K. Moradi, A. Salimi, M. Gholinejad, A. Feizabadi, Multi metallic electro-catalyst design for enhanced oxygen evolution reaction: immobilizing MnFe nanoparticles on ZIF-67-decorated graphene oxide, Electrochim. Acta 479 (2024) 143884.
[60] Z. Nagshbandi, M. Gholinejad, J.M. Sansano, Novel magnetic zeolitic imidazolate framework for room temperature enhanced catalysis, Inorg. Chem. Commun. 150 (2023) 110463.
[61] Y. Qiu, Y. Zhang, M. Yu, X. Li, Y. Wang, Z. Ma, S. Liu, Ni— co— O— S derived catalysts on hierarchical N-doped carbon supports with strong interfacial interactions for improved hybrid water splitting performance, Small 20 (29) (2024) 2310087.
[62] T. Ma, Y. Qiu, Y. Zhang, X. Ji, P.-A. Hu, Iron-doped Ni5P4 ultrathin nanoporous nanosheets for water splitting and on-demand hydrogen release via $NaBH_4$ hydrolysis, ACS Appl. Nano Mater. 2 (5) (2019) 3091–3099.
[63] Y. Qiu, X. Dai, Y. Wang, X. Ji, Z. Ma, S. Liu, The polyoxometalates mediated preparation of phosphate-modified $NiMoO_4$− x with abundant O-vacancies for H_2 production via urea electrolysis, J. Colloid Interface Sci. 629 (2023) 297–309.
[64] L.-L. Liu, L. Liu, C.-Y. Wang, L. Zhang, J.-J. Feng, Y.-J. Gao, A.-J. Wang, Strong coupling Fe2VO4 nanoparticles/3D N-doped interconnected porous carbon derived from MOFs by confined adsorption-assembly-pyrolysis for greatly boosting oxygen reduction, J. Colloid Interface Sci. 684 (2025) 10–20.
[65] Y. Liu, C. Tang, M. Cheng, M. Chen, S. Chen, L. Lei, Y. Chen, H. Yi, Y. Fu, L. Li, Polyoxometalate@ metal–organic framework composites as effective photocatalysts, ACS Catal. 11 (2021) 13374–13396.
[66] G. Paille, M. Gomez-Mingot, C. Roch-Marchal, M. Haouas, Y. Benseghir, T. Pino, M.-H. Ha-Thi, G. Landrot, P. Mialane, M. Fontecave, Thin films of fully noble metal-free POM@ MOF for photocatalytic water oxidation, ACS Appl. Mater. Interfaces 11 (2019) 47837–47845.
[67] J. Zou, M. Zheng, Z. Li, X. Zeng, J. Huang, Magnetization triggered oxygen evolution reaction enhancement for ferromagnetic materials, J. Mater. Sci. Mater. Electron. 33 (9) (2022) 6700–6709.
[68] Y. Yang, H. Yao, Z. Yu, S.M. Islam, H. He, M. Yuan, Y. Yue, K. Xu, W. Hao, G. Sun, Hierarchical nanoassembly of $MoS_2/Co_9S_8/Ni_3S_2$/Ni as a highly efficient electrocatalyst for overall water splitting in a wide pH range, JACS 141 (26) (2019) 10417–10430.
[69] J. Song, P. Zhu, W. Ma, Y. Li, PW_6Mo_6/ZIF-67@ NF composite with exposed co nodes as efficient oxygen evolution reaction electrocatalyst, Int. J. Hydrog. Energy 51 (2024) 327–337.
[70] X. Liu, J. Dong, B. You, Y. Sun, Competent overall water-splitting electrocatalysts derived from ZIF-67 grown on carbon cloth, RSC Adv. 6 (77) (2016) 73336–73342.
[71] Y.-J. Tang, H.-J. Zhu, L.-Z. Dong, A.-M. Zhang, S.-L. Li, J. Liu, Y.-Q. Lan, Solid-phase hot-pressing of POMs-ZIFs precursor and derived phosphide for overall water splitting, Appl. Catal. B Environ. 245 (2019) 528–535.
[72] Z. Liu, L. Yuan, T. Wen, J. Yu, X. Xu, Enhanced electrocatalytic activity of POM-derived CoMoS/FCP heterostructures for overall water splitting in alkaline media, Int. J. Electrochem. Sci. 18 (5) (2023) 100076.
[73] Y. Liu, S. Jiang, S. Li, L. Zhou, Z. Li, J. Li, M. Shao, Interface engineering of (Ni, Fe) S_2@ MoS_2 heterostructures for synergetic electrochemical water splitting, Appl. Catal. B Environ. 247 (2019) 107–114.
[74] L. Zhang, X. Ding, M. Cong, Y. Wang, X. Zhang, Self-adaptive amorphous Co_2P@ Co_2P/co-polyoxometalate/nickel foam as an effective electrode for electrocatalytic water splitting in alkaline electrolyte int, J. Hydrogen Energy. 44 (18) (2019) 9203–9209.
[75] H. Zhu, J. Zhang, R. Yanzhang, M. Du, Q. Wang, G. Gao, J. Wu, G. Wu, M. Zhang, B. Liu, When cubic cobalt sulfide meets layered molybdenum disulfide: a core–shell system toward synergetic electrocatalytic water splitting, Adv. Mater. 27 (32) (2015) 4752–4759.
[76] S. Chen, J. Duan, A. Vasileff, S.Z. Qiao, Size fractionation of two-dimensional sub-nanometer thin manganese dioxide crystals towards superior urea electrocatalytic conversion, Angew. Chem. Int. Ed. 55 (11) (2016) 3804–3808.
[77] J.-Y. Zhang, T. He, M. Wang, R. Qi, Y. Yan, Z. Dong, H. Liu, H. Wang, B.Y. Xia, Energy-saving hydrogen production coupling urea oxidation over a bifunctional nickel-molybdenum nanotube array, Nano Energy 60 (2019) 894–902.
[78] Y. Pan, K. Sun, Y. Lin, X. Cao, Y. Cheng, S. Liu, L. Zeng, W.-C. Cheong, D. Zhao, K. Wu, Electronic structure and d-band control engineering over M-doped CoP (M= Ni, Mn, Fe) hollow polyhedron frames for boosting hydrogen production, Nano Energy 56 (2019) 411–419.
[79] Z.-Y. Yu, C.-C. Lang, M.-R. Gao, Y. Chen, Q.-Q. Fu, Y. Duan, S.-H. Yu, Ni–Mo–O nanorod-derived composite catalysts for efficient alkaline water-to-hydrogen conversion via urea electrolysis, Energy Environ. Sci. 11 (7) (2018) 1890–1897.
[80] T. Wang, H. Wu, C. Feng, L. Zhang, J. Zhang, MoP@ NiCo-LDH on nickel foam as bifunctional electrocatalyst for high efficiency water and urea–water electrolysis, J Mater Chem A 8 (35) (2020) 18106–18116.
[81] X. Wang, J. Wang, X. Sun, S. Wei, L. Cui, W. Yang, J. Liu, Hierarchical coral-like NiMoS nanohybrids as highly efficient bifunctional electrocatalysts for overall urea electrolysis, Nano Res 11 (2018) 988–996.
[82] W.-K. Han, X.-P. Li, L.-N. Lu, T. Ouyang, K. Xiao, Z.-Q. Liu, Partial S substitution activates $NiMoO_4$ for efficient and stable electrocatalytic urea oxidation, Chem. Commun. 56 (75) (2020) 11038–11041.
[83] H. Cui, L. Gong, J. Wang, L. Dong, J. Zhang, Y. Mu, B. Yang, M. Wang, Y. Gu, H. Li, POM@ TM-MOFs prism-structures as a superior bifunctional electrocatalyst for overall water splitting, J. Solid State Chem. 331 (2024) 124550.
[84] Y. Zhang, Q. Shao, S. Long, X. Huang, Cobalt-molybdenum nanosheet arrays as highly efficient and stable earth-abundant electrocatalysts for overall water splitting, Nano Energy 45 (2018) 448–455.
[85] N. Li, Y. Guan, Y. Li, H. Mi, L. Deng, L. Sun, Q. Zhang, C. He, X. Ren, Co–Mo–P carbon nanospheres derived from metal–organic frameworks as a high-performance electrocatalyst towards efficient water splitting, J Mater Chem A 9 (2021) 1143–1149.
[86] J. Jiang, Q. Liu, C. Zeng, L. Ai, Cobalt/molybdenum carbide@ N-doped carbon as a bifunctional electrocatalyst for hydrogen and oxygen evolution reactions, J Mater Chem A 5 (2017) 16929–16935.
[87] S. Shit, S. Chhetri, W. Jang, N.C. Murmu, H. Koo, P. Samanta, T. Kuila, Cobalt sulfide/nickel sulfide heterostructure directly grown on nickel foam: an efficient and durable electrocatalyst for overall water splitting application, ACS Appl. Mater. Interfaces 10 (2018) 27712–27722.